Hindawi Publishing Corporation
EURASIP Journal on Wireless Communications and Networking
Volume 2007, Article ID 86206, 14 pages
doi:10.1155/2007/86206

Research Article

Comparison of OQPSK and CPM for Communications at 60 GHz with a Nonideal Front End

Jimmy Nsenga,[1,2] Wim Van Thillo,[1,2] François Horlin,[1] André Bourdoux,[1] and Rudy Lauwereins[1,2]

[1] *IMEC, Kapeldreef 75, 3001 Leuven, Belgium*
[2] *Departement Elektrotechniek - ESAT, Katholieke Universiteit Leuven, Kasteelpark Arenberg 10, 3001 Leuven, Belgium*

Received 4 May 2006; Revised 14 November 2006; Accepted 3 January 2007

Recommended by Su-Khiong Yong

Short-range digital communications at 60 GHz have recently received a lot of interest because of the huge bandwidth available at those frequencies. The capacity offered to the users could finally reach 2 Gbps, enabling the deployment of new multimedia applications. However, the design of analog components is critical, leading to a possible high nonideality of the front end (FE). The goal of this paper is to compare the suitability of two different air interfaces characterized by a low peak-to-average power ratio (PAPR) to support communications at 60 GHz. On one hand, we study the offset-QPSK (OQPSK) modulation combined with a channel frequency-domain equalization (FDE). On the other hand, we study the class of continuous phase modulations (CPM) combined with a channel time-domain equalizer (TDE). We evaluate their performance in terms of bit error rate (BER) considering a typical indoor propagation environment at 60 GHz. For both air interfaces, we analyze the degradation caused by the phase noise (PN) coming from the local oscillators; and by the clipping and quantization errors caused by the analog-to-digital converter (ADC); and finally by the nonlinearity in the PA.

1. INTRODUCTION

We are witnessing an explosive growth in the demand for wireless connectivity. Short-range wireless links like wireless local area networks (WLANs) and wireless personal area networks (WPANs) will soon be expected to deliver bit rates of over 1 Gbps to keep on satisfying this demand. Fast wireless download of multimedia content and streaming high-definition TV are two obvious examples. As lower frequencies (below 10 GHz) are getting completely congested though, bandwidth for these Gbps links has to be sought at higher frequencies. Recent regulation assigned a 3 GHz wide, worldwide available frequency band at 60 GHz to this kind of applications [1].

Communications at 60 GHz have some advantages as well as some disadvantages. The main advantages are threefold. The large unlicensed bandwidth around 60 GHz (more than 3 GHz wide) will enable very high data rate wireless applications. Secondly, the high free space path loss and high attenuation by walls simplify the frequency reuse over small distances. Thirdly, as the wavelength in free space is only 5 mm, the analog components can be made small. Therefore, on a small area, one can design an array of antennas, which steers the beam in a given target direction. This improves the link budget and reduces the time dispersion of the channel. Opposed to this are some disadvantages: the high path loss will restrict communications at 60 GHz to short distances, more stringent requirements are put on the analog components (like multi-Gsamples/s analog-to-digital converter ADC), and nonidealities of the radio frequency (RF) front end have a much larger impact than at lower frequencies. The design of circuits at millimeter waves is more problematic than at lower frequencies for two important reasons. First, the operating frequency is relatively close to the cut-off frequency and to the maximum oscillation frequency of nowadays' complementary metal oxide semiconductor (CMOS) transistors (e.g., the cut-off frequency of a transistor in a 90 nm state-of-the-art CMOS is around 150 GHz [2]), reducing significantly the design freedom. Second, the wavelength approaches the size of on-chip dimensions so that the interconnects have to be modeled as (lossy) transmission lines, complicating the modeling and circuit simulation and also the layout of the chip.

A suitable air interface for low-cost, low-power 60 GHz transceivers should thus use a modulation technique that has a high level of immunity to FE nonidealities (especially phase

noise (PN) and ADC quantization and clipping), and allows an efficient operation of the power amplifier (PA). Since the 60 GHz channel has been shown to be frequency selective for very large bandwidths and low antenna gains [3, 4], orthogonal frequency division multiplexing (OFDM) has been proposed for communications at 60 GHz. However, it is very sensitive to nonidealities such as PN and carrier frequency offset (CFO). Moreover, due to its high PAPR, it requires the PA to be backed off by several dB more than for a single carrier (SC) system, thus lowering the power efficiency of the system.

Therefore, we consider two other promising air interfaces that relax the FE requirements. First, we study an SC transmission scheme combined with OQPSK because it has a lower PAPR than regular QPSK or QAM in band-limited channels. As the multipath channel should be equalized at a low complexity, we add redundancy at the transmitter to make the signal cyclic and to be able to equalize the channel in the frequency domain [5]. Secondly, we study CPM techniques [6]. These have a perfectly constant amplitude, or a PAPR of 0 dB. Moreover, their continuous phase property results in lower spectral sidelobes. Linear representations and approximations developed by Laurent [7] and Rimoldi [8] allow for great complexity reductions in the equalization and detection processes. In order to mitigate the multipath channel, a conventional convolutive zero-forcing (ZF) equalizer is used.

The goal of this paper is to analyze, by means of simulations, the impact of three of the most critical building blocks in RF transceivers, and to compare the robustness of the two air interfaces to their nonideal behavior:

(i) the mixing stage where the local oscillator PN can be very high at 60 GHz,
(ii) the ADC that, for low-power consumption, must have the lowest possible resolution (number of bits) given the very high bit rate,
(iii) the PA where nonlinearities cause distortion and spectral regrowth.

The paper is organized as follows. In Section 2, we describe the indoor channel at 60 GHz. Section 3 describes the considered FE nonidealities. Sections 4 and 5 introduce the OQPSK and CPM air interfaces, respectively, together with their receiver design. Simulation setup and results are provided in Section 6 and the conclusions are drawn in Section 7.

Notation

We use roman letters to represent scalars, single underlined letters to denote column vectors, and double underlined letters to represent matrices. $[\cdot]^T$ and $[\cdot]^H$ stand for transpose and complex conjugate transpose operators, respectively. The symbol $\star$ denotes the convolution operation and $\otimes$ the Kronecker product. $\underline{\underline{I}}_k$ is the identity matrix of size $k \times k$ and $\underline{\underline{0}}_{m\times n}$ is an $m \times n$ matrix with all entries equal to 0.

2. THE INDOOR 60 GHZ CHANNEL

2.1. Propagation characteristics

The interest in the 60 GHz band is motivated by the large amount of unlicensed bandwidth located between 57 and 64 GHz [1, 9]. Analyzing the spectrum allocation in the United States (US), Japan, and Europe, one notices that there is a common contiguous 3 GHz bandwidth between 59 and 62 GHz that has been reserved for high data rate applications. This large amount of bandwidth can be exploited to establish a wireless connection at more than 1 Gbps.

Different measurement campaigns have been carried out to characterize the 60 GHz channel. The free space loss (FSL) can be computed using the Friis formula (1) as follows:

$$\text{FSL [dB]} = 20 \times \log_{10}\left(\frac{4\pi d}{\lambda}\right), \tag{1}$$

where λ is signal wavelength and d is the distance of the terminal from the transmitter base station. One can see that the FLS is already 68 dB at 1 m separation away from the transmitter. Thus, given the limited transmitted power, the communication range will hardly extend over 10 m. Besides the FSL, reflection and penetration losses of objects at 60 GHz are higher than at lower frequencies [10, 11]. For instance, concrete walls 15 cm thick attenuate the signal by 36 dB. They act thus as real boundaries between different rooms.

However, the signals reflected off the concrete walls have a sufficient amplitude to contribute to the total received power, thus making the 60 GHz channel a multipath channel [3, 12]. Typical root mean-square (RMS) delay spreads at 60 GHz can vary from 10 nanoseconds to 100 nanoseconds if omni-directional antennas are used, depending on the dimensions and reflectivity of the environment [3]. However, the RMS delay spread can be greatly reduced to less than 1 nanosecond by using directional antennas, thus increasing the coherence bandwidth of the channel up to 200 MHz [13].

Moreover, the objects moving within the communication environment make the channel variant over time. Typical values of Doppler spread at 60 GHz are around 200 Hz at a normal walking speed of 1 millisecond. This results in a coherence time of approximatively 1 millisecond. With a symbol period of 1 nanosecond, 10^6 symbols can be transmitted in a quasistatic environment. Thus, Doppler spread at 60 GHz will not have a significant impact on the system performance.

In summary, 60 GHz communications are mainly suitable for short-range communications due to the high propagation loss. The channel is frequency selective due to the large bandwidth used (more than 1 GHz). However, one can assume the channel to be time invariant during the transmission of one block.

2.2. Channel model

In this study, we model the indoor channel at 60 GHz using the Saleh-Valenzuela model [14], which assumes that the

received signals arrive in clusters. The rays within a cluster have independent uniform phases. They also have independent Rayleigh amplitudes whose variances decay exponentially with cluster and rays delays. In the Saleh-Valenzuela model, the cluster decay factor is denoted by Γ and the rays decay factor is represented by γ. The clusters and the rays form Poisson arrival processes that have different, but fixed rates Λ and λ, respectively [14].

We consider the same scenario as that defined in [15]. The base station has an omni-directional antenna with 120° beam width and is located in the center of the room. The remote station has an omni-directional antenna with 60° beam width and is placed at the edge of the room. The corresponding Saleh-Valenzuela parameters are presented in Table 1.

Table 1: Saleh-Valenzuela channel parameters at 60 GHz.

$1/\Lambda$	75 nanoseconds
Γ	20 nanoseconds
$1/\lambda$	5 nanoseconds
γ	9 nanoseconds

3. NONIDEALITIES IN ANALOG TRANSCEIVERS

In this section, we introduce 3 FE nonidealities: ADC clipping and quantization, PN and nonlinearity of the PA. The rationale for choosing these 3 nonidealities is that a good PA, a high resolution ADC, and a low PN oscillator have a high power consumption [16].

3.1. Clipping and quantization

3.1.1. Motivation

The number of bits (NOB) of the ADC must be kept as low as possible for obvious reasons of cost and power consumption. On the other hand, a large number of bits is desirable to reduce the effect of quantization noise and the risk of clipping the signal. Clipping occurs when the signal fluctuation is larger than the dynamic range of the ADC. Without going into detail, we mention that there is always an optimal clipping level for a given NOB. As the clipping level is increased, the signal degradation due to clipping is reduced. However, the degradation due to quantization is increased as a larger dynamic range must be covered with the same NOB. For a more elaborate discussion, we refer to [17].

3.1.2. Model

The ADC is thus characterized by two parameters: the NOB and the normalized clipping level μ, which is the ratio of the clipping level to the RMS value of the amplitude of the signal. In Figure 1, we illustrate the clipping/quantization function for an NOB = 3. This simple model is used in our simulations in Section 6.4.

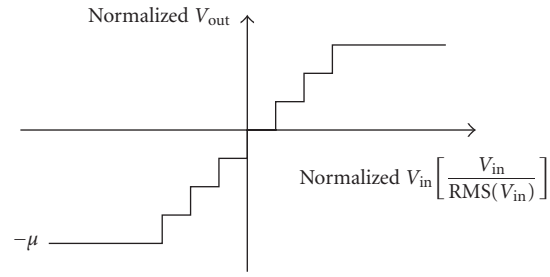

Figure 1: ADC input-output characteristic.

3.2. Phase noise

3.2.1. Motivation

PN originates from nonideal clock oscillators, voltage-controlled oscillators (VCO), and frequency synthesis circuits. In the frequency domain, PN is most often characterized by the power spectral density (PSD) of the the oscillator phase $\phi(t)$. The PSD of an ideal oscillator has only a Dirac pulse at its carrier frequency, corresponding to no phase fluctuation at all. In practice, the PSD of the phase exhibits a 20 dB/dec decreasing behavior as the offset from the carrier frequency increases. Nonmonotonic behavior is attributable to, for example, phase-locked loop (PLL) filters in the frequency synthesis circuit.

3.2.2. Model

We characterize the phase noise by a set of 3 parameters (see Figure 2) [18]:

(i) the integrated PSD denoted K, expressed in dBc, which is the two-sided integral of the phase noise PSD,
(ii) the 3 dB bandwidth,
(iii) the VCO noise floor.

Note that these 3 parameters will fix the value of the PN PSD at low frequency offsets. In our simulations (see Section 6.3), we assume a phase noise bandwidth of 1 MHz and a noise floor of −130 dBc/Hz. Typical values of the level of PN PSD at 1 MHz are considered [19] and the corresponding integrated PSD is calculated in Table 2. In order to generate a phase noise characterized by the PSD illustrated in Figure 2, a white Gaussian noise is convolved with a filter whose frequency domain response is equal to the square root of the PSD.

3.3. Nonlinear power amplification

3.3.1. Motivation

Nonlinear behavior can occur in any amplifier but it is more likely to occur in the last amplifier of the transmitter where the signal power is the highest. For power consumption reasons, this amplifier must have a saturated output power that is as low as possible, compatible with the system level constraints such as transmit power and link budget. The gain characteristic of an amplifier is almost perfectly linear at low

Table 2: Simulated integrated PSD.

PN @1 MHz [dBc/Hz]	Integrated PSD [dBc]
−90	−24
−85	−20
−82	−16

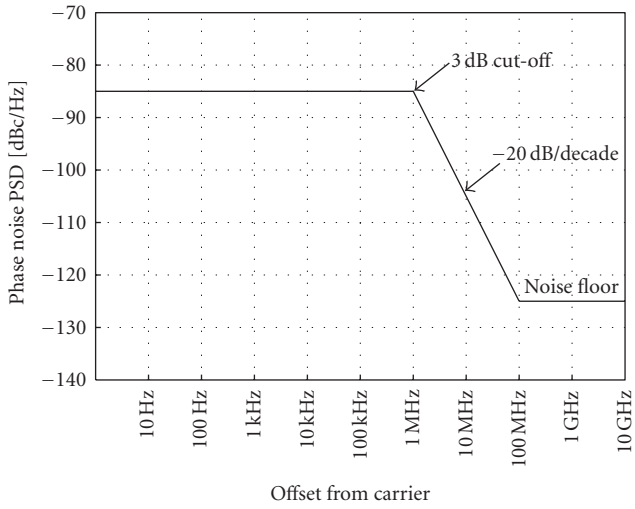

Figure 2: Piecewise linear phase noise PSD definition used in the phase noise model.

input level and, for increasing input power, deviates from the linear behavior as the input power approaches the 1-dB compression point ($P_{1\,\mathrm{dB}}$: the point at which the gain is reduced by 1-dB because the amplifier is driven into saturation) and eventually reaches complete saturation. The input third-order intercept point (IP_3) is also often used to quantify the nonlinear behavior of amplifiers. It is the input power at which the power of the two-tone third-order intermodulation product would become equal to the power of the first-order term. When peaks are present in the transmitted waveform, one has to operate the PA with a few dBs of backoff to prevent distortion. This backoff actually reduces the power efficiency of the PA and must be kept to a minimum.

3.3.2. Model

In our simulation (see Section 6.5), we characterize the nonlinearity of the PA by a third-order nonlinear equation

$$y(t) = a_1 x(t) + a_3 \left| x(t) \right|^2 x(t), \tag{2}$$

where $x(t)$ and $y(t)$ are the baseband equivalent PA input and output, respectively, a_1 and a_3 are real polynomial coefficients. We assume an amplifier with a unity gain ($a_1 = 1$) and an input amplitude at 1-dB compression point $A_{1\mathrm{dB}}$ normalized to 1. Therefore, by using (3), one can compute the third-order coefficient a_3

$$a_3 = -0.145 \frac{a_1}{A_{1\,\mathrm{dB}}^2}. \tag{3}$$

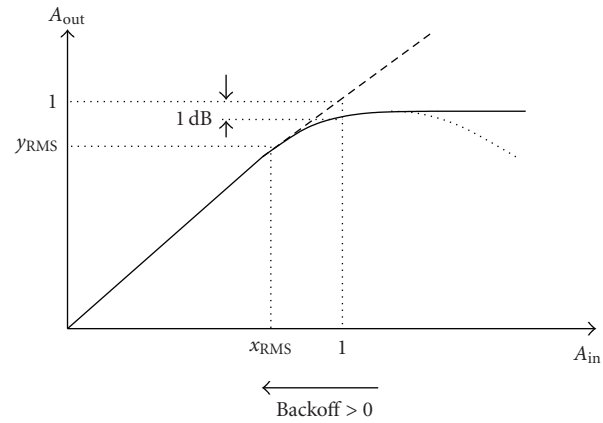

Figure 3: PA input-output power characteristic.

The parameter a_3 is then equal to −0.145. Note that (2) models only the amplitude-to-amplitude (AM-AM) conversion of a nonlinear PA. In order to make our model more realistic, a saturation level is set from the extremum of the cubic function. The root mean-square (RMS) value of the input PA signal is computed and its level is adapted according to the backoff requirement. The backoff is defined relative to $A_{1\,\mathrm{dB}}$ and is the only varying parameter. Then the nonlinearity is introduced using the AM-AM conversion as shown in Figure 3.

4. OFFSET QPSK WITH FREQUENCY DOMAIN EQUALIZATION

4.1. Initial concept

Offset-QPSK, a variant of QPSK digital modulation, is characterized by a half symbol period delay between the data mapped on the quadrature (Q) branch and the one mapped on the inphase (I) branch. This offset imposes that either the I or the Q signal changes during the half symbol period. Consequently, the phase shift between two consecutive OQPSK symbols is limited to ±90° (±180° in conventional QPSK modulation), thus avoiding the amplitude of the signal to go through the "0" point. The advantage of an OQPSK modulated signal over QPSK signal is observed in band-limited channels where nonrectangular pulse shaping, for instance, root raised root cosine, is used. The envelope fluctuation of an OQPSK signal is found to be 70% lower than that of a conventional QPSK signal [20]. Thus, OQPSK is considered to be a low PAPR modulation scheme, for which a nonlinear PA with less backoff can be used, thus increasing the power efficiency of the system.

4.2. System model

Our system model is inspired from the model of Wang and Giannakis [21]. Let us consider the baseband block transmitter model represented in Figure 4. The inphase component of the digital OQPSK signal is denoted by $u_I[k]$ and

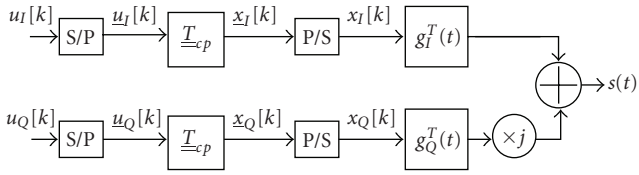

Figure 4: Offset QPSK block transmission.

the quadrature-phase component denoted by $u_Q[k]$. The two streams are first serial-to-parallel (S/P) converted to form blocks $\underline{u}_I[k] := [u_I[kB], u_I[kB+1], \ldots, u_I[kB+B-1]]^T$ and $\underline{u}_Q[k] := [u_Q[kB], u_Q[kB+1], \ldots, u_Q[kB+B-1]]^T$ where B is the block size. Then, a cyclic prefix (CP) of length N_{cp} is inserted at the beginning of each block to get cyclic blocks $\underline{x}_I[k]$ and $\underline{x}_Q[k]$. The cyclic prefix insertion is done by multiplying both $\underline{u}_I[k]$ and $\underline{u}_Q[k]$ with the matrix $\underline{\underline{T}}_{\text{cp}} = [\underline{\underline{0}}_{N_{\text{cp}}\times(B-N_{\text{cp}})}, \underline{\underline{I}}_{N_{\text{cp}}}; \underline{\underline{I}}_B]$ of size $(B+N_{\text{cp}})\times B$. In a practical system, the N_{cp} should be larger than the channel impulse response length, and the size of the block B is chosen so that the CP overhead is limited (practically an overhead of 1/5 is often used). The size B should on the other hand be as small as possible to reduce the complexity and to ensure that the channel is constant within one symbol block duration. The cyclic blocks $\underline{x}_I[k]$ and $\underline{x}_Q[k]$ are afterwards converted back to serial streams and the resulting streams $x_I[k]$ and $x_Q[k]$ of sample duration equal to T are filtered by square root raised cosine filters $g_I^T(t)$ and $g_Q^T(t)$, respectively. The inherent offset between I and Q branches, which differentiates the OQPSK signaling from the normal QPSK, is modeled through the pulse-shaping filters defined such that $g_Q^T(t) = g_I^T(t - T/2)$. The two pulse-shaped signals are then summed together to form the equivalent complex lowpass transmitted signal $s(t)$.

The signal $s(t)$ is then transmitted through a frequency selective channel, which we model by its equivalent lowpass channel impulse response $c(t)$. Figure 5 shows a block diagram of the receiver. The received signal $r_{\text{in}}(t)$ is corrupted by additive white Gaussian noise (AWGN), $n(t)$, generated by analog FE components. The noisy received signal is first lowpass-filtered by an anti-aliasing filter with ideal lowpass specifications before the discretization. We consider the following two sample rates.

(i) The nonfractional sampling (NFS) rate which corresponds to sampling the analog signal every T seconds. The corresponding anti-aliasing filter, denoted $g_{\text{NFS}}^R(t)$, eliminates all the frequencies above $0.5/T$.

(ii) The fractional sampling (FS) rate for which the sampling period is $T/2$ seconds. The cutoff frequency of the anti-aliasing filter $g_{\text{FS}}^R(t)$ is set to $1/T$.

More information about the two sampling modes can be found in [22]. In the sequel, we focus on the FS case. The NFS can be seen as a special case of FS. In order to characterize the received signal, we define $h_I(t) := g_I^T(t) \star c(t) \star g_{\text{FS}}^R(t)$ and $h_Q(t) := j * g_Q^T(t) \star c(t) \star g_{\text{FS}}^R(t)$ as the overall channel impulse response encountered by data symbols on I and Q, respectively. The received signal after lowpass filtering is given by

$$r(t) = \sum_k x_I[k] h_I(t - kT) + \sum_k x_Q[k] h_Q(t - kT) + v(t) \tag{4}$$

in which $v(t)$ is the lowpass filtered noise. The analog received signal $r(t)$ is then sampled every $T/2$ seconds to get the discrete-time sequence $r[m]$.

As explained in [22], fractionally sampled signals are processed by creating polyphase components, where even and odd indexed samples of the received signal are separated. In the following, the index "0" is related to even samples or polyphase component "0" while odd samples are represented by index "1" or polyphase component "1." Thus, we define

$$\begin{aligned} r^\rho[m] &\stackrel{\text{def}}{=} r[2m+\rho], \\ v^\rho[m] &\stackrel{\text{def}}{=} v[2m+\rho], \\ h_I^\rho[m] &\stackrel{\text{def}}{=} h_I[2m+\rho], \\ h_Q^\rho[m] &\stackrel{\text{def}}{=} h_Q[2m+\rho], \end{aligned} \tag{5}$$

where ρ denotes either the polyphase component "0" or the polyphase component "1," $r[m]$ and $v[m]$ are, respectively, the received signal $r(t)$ and the noise $v(t)$ sampled every $T/2$ seconds, $h_I[m]$ and $h_Q[m]$ represent the discrete-time version of, respectively, $h_I(t)$ and $h_Q(t)$ sampled every $T/2$ seconds. The sampled channels $h_I^\rho[m]$ and $h_Q^\rho[m]$ have finite impulse responses, of length L_I and L_Q, respectively. These time dispersions cause the intersymbol interference (ISI) between consecutive symbols, which, if not mitigated, degrades the performance of the system. Next to the separation in polyphase components, we separate the real and imaginary parts of different polyphase signals. Starting from now, we use the supplementary upper index $c = \{r, i\}$ to identify the real or imaginary parts of the sequences.

The four real-valued sequences $r^{\rho c}[m]$ are serial to parallel converted to obtain the blocks $\underline{r}^{\rho c}[m] := [r^{\rho c}[mB], r^{\rho c}[mB+1], \ldots, r^{\rho c}[mB+B+N_{\text{cp}}-1]]^T$ of $(B+N_{\text{cp}})$ samples. The corresponding transmit-receive block relationship, assuming a correct time and frequency synchronization, is given by

$$\begin{aligned} \underline{r}^{\rho c}[m] = {} & \underline{\underline{H}}_I^{\rho c}[0]\underline{\underline{T}}_{\text{cp}}\underline{u}_I[m] + \underline{\underline{H}}_I^{\rho c}[1]\underline{\underline{T}}_{\text{cp}}\underline{u}_I[m-1] \\ & + \underline{\underline{H}}_Q^{\rho c}[0]\underline{\underline{T}}_{\text{cp}}\underline{u}_Q[m] + \underline{\underline{H}}_Q^{\rho c}[1]\underline{\underline{T}}_{\text{cp}}\underline{u}_Q[m-1] \\ & + \underline{v}^{\rho c}[m], \end{aligned} \tag{6}$$

where $\underline{v}^{\rho c}[m]$ is the mth filtered noise block defined as $\underline{v}^{\rho c}[m] := [v^{\rho c}[mB], v^{\rho c}[mB+1], \ldots, v^{\rho c}[mB+B+N_{\text{cp}}-1]]^T$. The square matrices $\underline{\underline{H}}_X^{\rho c}[0]$ and $\underline{\underline{H}}_X^{\rho c}[1]$ of size $(B+N_{\text{cp}})\times(B+N_{\text{cp}})$, with X equal to I or Q, are represented in the following

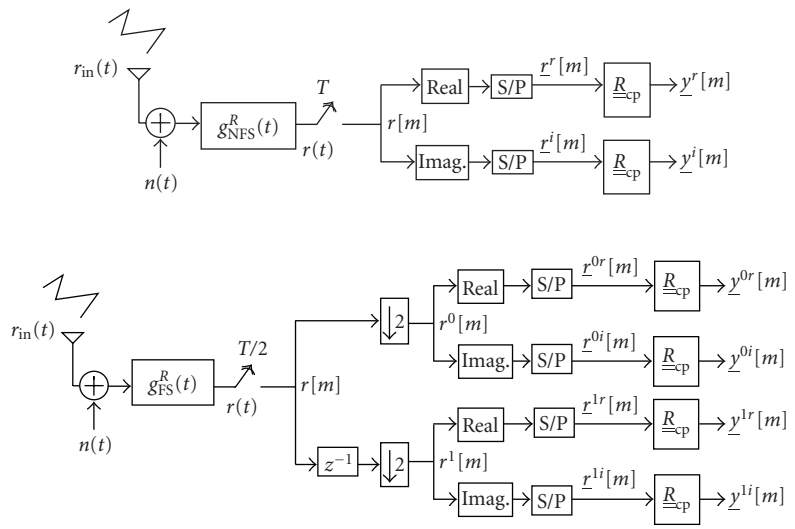

Figure 5: Receiver: upper part NFS, lower part FS.

equations:

$$\underline{\underline{H}}_X^{\rho c}[0] = \begin{bmatrix} h_X^{\rho c}[0] & 0 & 0 & \cdots & 0 \\ \vdots & h_X^{\rho c}[0] & 0 & \cdots & 0 \\ h_X^{\rho c}[L_X] & \cdots & \ddots & \cdots & 0 \\ \vdots & \ddots & \cdots & \ddots & 0 \\ 0 & \cdots & h_X^{\rho c}[L_X] & \cdots & h_X^{\rho c}[0] \end{bmatrix},$$

$$\underline{\underline{H}}_X^{\rho c}[1] = \begin{bmatrix} 0 & \cdots & h_X^{\rho c}[L_X] & \cdots & h_X^{\rho c}[1] \\ \vdots & \ddots & 0 & \ddots & \vdots \\ 0 & \cdots & \ddots & \cdots & h_X^{\rho c}[L_X] \\ \vdots & \vdots & \cdots & \ddots & \vdots \\ 0 & \cdots & 0 & \cdots & 0 \end{bmatrix}. \tag{7}$$

The second and the fourth terms in (6) highlight the inter-block interference (IBI) that arises between consecutive blocks due to the time dispersion of the channel. The IBI between consecutive blocks $\underline{u}_I[m]$ or $\underline{u}_Q[m]$ is afterwards eliminated by discarding the first N_{cp} samples in each received block. This operation is carried out by multiplying the received blocks in (6) by a guard removal matrix $\underline{\underline{R}}_{\text{cp}} = [\underline{\underline{0}}_{B\times N_{\text{cp}}}, \underline{\underline{I}}_B]$ of size $B \times (B + N_{\text{cp}})$. We get

$$\begin{aligned} \underline{y}^{\rho c}[m] \overset{\text{def}}{=} \underline{\underline{R}}_{\text{cp}}\, \underline{r}^{\rho c}[m] &= \underline{\underline{R}}_{\text{cp}}\, \underline{\underline{H}}_I^{\rho c}[0] \underline{\underline{T}}_{\text{cp}}\, \underline{u}_I[m] \\ &+ \underline{\underline{R}}_{\text{cp}}\, \underline{\underline{H}}_I^{\rho c}[1] \underline{\underline{T}}_{\text{cp}}\, \underline{u}_I[m-1] + \underline{\underline{R}}_{\text{cp}}\, \underline{\underline{H}}_Q^{\rho c}[0] \underline{\underline{T}}_{\text{cp}}\, \underline{u}_Q[m] \\ &+ \underline{\underline{R}}_{\text{cp}}\, \underline{\underline{H}}_Q^{\rho c}[1] \underline{\underline{T}}_{\text{cp}}\, \underline{u}_Q[m-1] + \underline{\underline{R}}_{\text{cp}}\, \underline{v}^{\rho c}[m]. \end{aligned} \tag{8}$$

As N_{cp} has been chosen to be larger than the $\max\{L_I, L_Q\}$, the product of $\underline{\underline{R}}_{\text{cp}}$ and each of $\underline{\underline{H}}_I^{\rho c}[1]$ and $\underline{\underline{H}}_Q^{\rho c}[1]$ matrices is null. Moreover, the left and right cyclic prefix insertion and removal operations around $\underline{\underline{H}}_I^{\rho c}[0]$ and $\underline{\underline{H}}_Q^{\rho c}[0]$, described mathematically as $\underline{\underline{R}}_{\text{cp}}\, \underline{\underline{H}}_I^{\rho c}[0] \underline{\underline{T}}_{\text{cp}}$ and $\underline{\underline{R}}_{\text{cp}}\, \underline{\underline{H}}_Q^{\rho c}[0] \underline{\underline{T}}_{\text{cp}}$, respectively, result in circulant matrices $\dot{\underline{\underline{H}}}_I^{\rho c}$ and $\dot{\underline{\underline{H}}}_Q^{\rho c}$ of size $(B \times B)$. Finally, the discrete-time block input-output relationship taking the CP insertion and removal operations into account is

$$\underline{y}^{\rho c}[m] = \dot{\underline{\underline{H}}}_I^{\rho c}\, \underline{u}_I[m] + \dot{\underline{\underline{H}}}_Q^{\rho c}\, \underline{u}_Q[m] + \underline{w}^{\rho c}[m] \tag{9}$$

in which $\underline{w}^{\rho c}[m]$ is obtained by discarding the first N_{cp} samples from the filtered noise block $\underline{v}^{\rho c}[m]$. By stacking the real and the imaginary parts of the two polyphase components on top of each other, the matrix representation of the FS case is

$$\underbrace{\begin{bmatrix} \underline{y}^{0r}[m] \\ \underline{y}^{0i}[m] \\ \underline{y}^{1r}[m] \\ \underline{y}^{1i}[m] \end{bmatrix}}_{\underline{y}[m]} = \underbrace{\begin{bmatrix} \dot{\underline{\underline{H}}}_I^{0r} & \dot{\underline{\underline{H}}}_Q^{0r} \\ \dot{\underline{\underline{H}}}_I^{0i} & \dot{\underline{\underline{H}}}_Q^{0i} \\ \dot{\underline{\underline{H}}}_I^{1r} & \dot{\underline{\underline{H}}}_Q^{1r} \\ \dot{\underline{\underline{H}}}_I^{1i} & \dot{\underline{\underline{H}}}_Q^{1i} \end{bmatrix}}_{\dot{\underline{\underline{H}}}} \underbrace{\begin{bmatrix} \underline{u}_I[m] \\ \underline{u}_Q[m] \end{bmatrix}}_{\underline{u}[m]} + \underbrace{\begin{bmatrix} \underline{w}^{0r}[m] \\ \underline{w}^{0i}[m] \\ \underline{w}^{1r}[m] \\ \underline{w}^{1i}[m] \end{bmatrix}}_{\underline{w}[m]}. \tag{10}$$

Finally, we get

$$\underline{y}[m] = \dot{\underline{\underline{H}}}\, \underline{u}[m] + \underline{w}[m] \tag{11}$$

in which $\underline{y}[m]$ denotes the compound received signal, $\underline{u}[m]$ is a vector containing both the I and Q transmitted symbols, and $\underline{w}[m]$ denotes the noise vector, $\dot{\underline{\underline{H}}}$ is the compound channel matrix. The vectors $\underline{y}[m]$ and $\underline{w}[m]$ contain $4B$ symbols, $\dot{\underline{\underline{H}}}$ is a matrix of size $4B \times 2B$, and $\underline{u}[m]$ is a vector of $2B$ symbols. Notice that all these vectors and matrices are real valued. Interestingly, the NFS case can be obtained from the FS by the two following adaptations.

(i) First, one has to change the analog anti-aliasing filter at the receiver. In fact, the cut-off frequency of the NFS filter is $0.5/T$ while it is $1/T$ for the FS filter.

(ii) Second, one keeps only the polyphase component with superscript index "0" in (10).

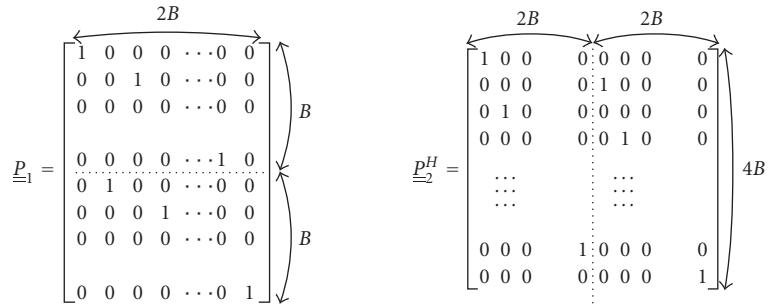

Figure 6: Permutation matrices $\underline{\underline{P}}$ and $\underline{\underline{P}}^H$.

At this point, even as the IBI has been eliminated between consecutive blocks, ISI within each individual block is still present. However, the IBI-free property of the resulting blocks allow to equalize each block independently from the others. In the following, we design an FDE to mitigate the remaining ISI.

4.3. Frequency domain equalization

According to [23], the expression of a linear minimum mean-square error (MMSE) detector that multiplies the received signal $\underline{y}[m]$ to provide the estimation $\underline{\hat{u}}[m]$ of the vector of transmitted symbols is given by

$$\underline{\underline{Z}}_{\text{MMSE}} = \left[\frac{\sigma_w^2}{\sigma_u^2}\underline{\underline{I}}_{2B} + \underline{\underline{\dot{H}}}^H \underline{\underline{\dot{H}}}\right]^{-1} \underline{\underline{\dot{H}}}^H, \tag{12}$$

where σ_u^2 and σ_w^2 represent the variances of the real and imaginary parts of the transmitted symbols and of the AWGN, respectively. However, the computation of this expression is very complex due to the structure of $\underline{\underline{\dot{H}}}$. Fortunately, by exploiting the properties of the circulant matrices composing $\underline{\underline{\dot{H}}}$, the latter can be transformed in a matrix $\underline{\underline{\Lambda}}$ (of the same size as $\underline{\underline{\dot{H}}}$) of diagonal submatrices, by the discrete block Fourier transform matrices $\underline{\underline{\mathcal{F}}}_m$ and $\underline{\underline{\mathcal{F}}}_n^H$ defined as

$$\underline{\underline{\dot{H}}} = \underline{\underline{\mathcal{F}}}_n^H \underline{\underline{\Lambda}}\, \underline{\underline{\mathcal{F}}}_m, \tag{13}$$

$$\begin{aligned} \underline{\underline{\mathcal{F}}}_m &\overset{\text{def}}{=} \underline{\underline{F}} \otimes \underline{\underline{I}}_m, \\ \underline{\underline{\mathcal{F}}}_n^H &\overset{\text{def}}{=} \underline{\underline{F}}^H \otimes \underline{\underline{I}}_n, \end{aligned} \tag{14}$$

where $\underline{\underline{F}}$ is the discrete Fourier transform matrix of size $B \times B$. For the FS case, $m = 2$ and $n = 4$ while in the NFS case $m = n = 2$. Note that $\underline{\underline{F}}_m$ and $\underline{\underline{F}}_n$ are square matrices of size $mB \times mB$ and $nB \times nB$, respectively. The different diagonal matrices are denoted by $\underline{\underline{\Lambda}}_X^{\rho c}$, and their diagonals are calculated by

$$\text{diag}(\underline{\underline{\Lambda}}_X^{\rho c}) = \frac{1}{\sqrt{B}} \cdot \underline{\underline{F}} \cdot \underline{h}_X^{\rho c} \tag{15}$$

with $\underline{h}_X^{\rho c} = [h_X^{\rho c}[0], h_X^{\rho c}[1], \ldots, h_X^{\rho c}[L_X]]^T$.

In addition to the frequency domain transformation, a permutation between columns and lines of $\underline{\underline{\Lambda}}$ is performed to simplify the complexity of the matrix inversion operation. The permutation is realized such that $\underline{\underline{\Lambda}}$ is transformed into a block diagonal matrix $\underline{\underline{\Psi}}$ (see Figure 7). The lth block $\underline{\underline{\Psi}}_l$ contains the lth subcarrier frequency response $\lambda_{X,l}^{\rho c}$ of the different channels; thus each subcarrier is equalized individually and independently from the others. We obtain

$$\underline{\underline{\Psi}} = \begin{bmatrix} \underline{\underline{\Psi}}_1 & & & \bigcirc \\ & \underline{\underline{\Psi}}_2 & & \\ & & \ddots & \\ & & \underline{\underline{\Psi}}_l & \\ \bigcirc & & & \ddots \\ & & & \underline{\underline{\Psi}}_B \end{bmatrix} \quad \text{with } \underline{\underline{\Psi}}_l = \begin{bmatrix} \lambda_{I,l}^{0r} & \lambda_{Q,l}^{0r} \\ \lambda_{I,l}^{0i} & \lambda_{Q,l}^{0i} \\ \lambda_{I,l}^{1r} & \lambda_{Q,l}^{1r} \\ \lambda_{I,l}^{1i} & \lambda_{Q,l}^{1i} \end{bmatrix}$$

Figure 7: Block diagonal matrix.

$$\underline{\underline{\Lambda}} = \underline{\underline{P}}_2^H \underline{\underline{\Psi}}\, \underline{\underline{P}}_1, \tag{16}$$

where the permutation matrices $\underline{\underline{P}}_1$ and $\underline{\underline{P}}_2^H$ are defined as shown in Figure 6

Finally, by replacing (16) and (13) in (12), the expression of the joint MMSE detector becomes

$$\underline{\underline{Z}}_{\text{MMSE}} = \underline{\underline{\mathcal{F}}}_n^H \underline{\underline{P}}_2^H \left[\frac{\sigma_w^2}{\sigma_u^2}\underline{\underline{I}} + \underline{\underline{\Psi}}^H \underline{\underline{\Psi}}\right]^{-1} \underline{\underline{\Psi}}^H \underline{\underline{P}}_1 \underline{\underline{\mathcal{F}}}_m. \tag{17}$$

From (17), one derives the expression of the joint zero forcing (ZF) detector by assuming a very high signal-to-noise ratio (SNR), whereby the term σ_w^2/σ_u^2 becomes negligible [23]:

$$\underline{\underline{Z}}_{\text{ZF}} = \underline{\underline{\mathcal{F}}}_n^H \underline{\underline{P}}_2^H [\underline{\underline{\Psi}}^H \underline{\underline{\Psi}}]^{-1} \underline{\underline{\Psi}}^H \underline{\underline{P}}_1 \underline{\underline{\mathcal{F}}}_m. \tag{18}$$

The complexity in terms of number of operations (NOPS) of the FD equalizer computation and the equalization is assessed in Tables 3 and 4, respectively. The complexity of an FFT of size B is proportional to $(B/2)\log_2 B$. The NFS case is much less complex than the FS. It is well known that the complexity of the FDE is much smaller than the complexity of the TDE (the inversion of the inner matrix necessary to compute the equalizer and the multiplication of the received vector by this equalizer would be both proportional to B^3).

Table 3: Equalizer computation.

Task	Operation	NOPS	
		FS	NFS
Computation of $\mathrm{diag}(\underline{\underline{\Lambda}}_X^{\rho c})$	FFT	8	4
Computation of $[\underline{\underline{\Psi}}^H \underline{\underline{\Psi}}]^{-1} \underline{\underline{\Psi}}^H$	+ and ×	$8B$	$4B$

Table 4: Equalization.

Task	Operation	NOPS	
		FS	NFS
Frequency components of $\underline{y}^{\rho c}[m]$	FFT	4	2
Equalization	+ and ×	$14B$	$6B$
Equalized symbols in time domain	IFFT	2	2

5. CONTINUOUS PHASE MODULATION

5.1. Transmitted signal

CPM covers a large class of modulation schemes with a constant amplitude, defined by

$$s(t,\underline{a}) = \sqrt{\frac{2E_S}{T}} e^{j\phi(t,\underline{a})}, \tag{19}$$

where $s(t,\underline{a})$ is the sent complex baseband signal, E_S the energy per symbol, T the symbol duration, and $\underline{a} = [a[0], a[1], \ldots, a[N-1]]$ is a vector of length N containing the sequence of M-ary data symbols $a[n] = \pm 1, \pm 3, \ldots, \pm(M-1)$. The transmitted information is contained in the phase

$$\phi(t,\underline{a}) = 2\pi h \sum_{n=0}^{N-1} a[n] \cdot q(t-nT), \tag{20}$$

where h is the modulation index and

$$q(t) = \int_{-\infty}^{t} g(\tau) d\tau. \tag{21}$$

Normally the function $g(t)$ is a smooth pulse shape over a finite time interval $0 \le t \le LT$ and zero outside. Thus L is the length of the pulse per unit T. The function $g(t)$ is normalized such that $\int_{-\infty}^{\infty} g(t)dt = 1/2$. This means that for schemes with positive pulses of finite length, the maximum phase change over any symbol interval is $(M-1)h\pi$.

As shown in [24], the BER can be halved by precoding the information sequence before passing it through the CPM modulator. If $\underline{d} = [d[1], d[2], \ldots, d[N-1]]$ is a vector containing the uncoded input bipolar symbol stream, the output of the precoder $\underline{a}$ (assuming $M = 2$) can be written as

$$a[n] = d[n] \cdot d[n-1], \tag{22}$$

where $d[-1] = 1$.

A conceptual general transmitter structure based on (19) and (22) is shown in Figure 8.

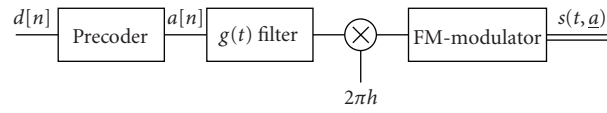

Figure 8: Conceptual modulator for CPM.

5.2. GMSK for low-cost, low-power 60 GHz transmitters

GMSK has been adopted as the modulation scheme for the European GSM system and for Bluetooth due to its spectral efficiency and constant-envelope property [25]. These two characteristics result in superior performance in the presence of adjacent channel interference and nonlinear amplifiers [24], making it a very attractive scheme for 60 GHz applications too. GMSK is obtained by choosing a Gaussian frequency pulse

$$g(t) = Q\left(\frac{2\pi B_T (t - T/2)}{\sqrt{\ln 2}}\right) - Q\left(\frac{2\pi B_T (t + T/2)}{\sqrt{\ln 2}}\right), \tag{23}$$

where $Q(x)$ is the well-known *error function* and B_T is the *bandwidth parameter*, which represents the −3 dB bandwidth of the Gaussian pulse. We will focus on a GMSK scheme with *time-bandwidth product* $B_T T = 0.3$, which enables us to truncate the Gaussian pulse to $L = 3$ without significantly influencing the spectral properties [26]. A modulation index $h = 1/2$ is chosen as this enables the use of simple MSK-type receivers [27]. The number of symbol levels is chosen as $M = 2$.

5.3. Linear representation by Laurent

Laurent [7] showed that a binary partial-response CPM signal can be represented as a linear combination of 2^{L-1} amplitude modulated pulses $C_k(t)$ (with $t = NT + \tau$, $0 \le \tau < T$):

$$s(t,\underline{a}) = \sum_{n=0}^{N-1} \sum_{k=0}^{2^{L-1}-1} e^{j\pi h \alpha_k[n]} C_k(t - nT), \tag{24}$$

where

$$\begin{aligned} C_k(t-nT) &= S(t) \cdot \prod_{n=1}^{L-1} S\big(t + (n + L\beta_{n,k})T\big), \\ \alpha_k[n] &= \sum_{m=0}^{n} a[m] - \sum_{m=1}^{L-1} a[n-m]\beta_{n,k}, \end{aligned} \tag{25}$$

and $\beta_{n,k} = 0, 1$ are the coefficients of the binary representation of the index k such that

$$k = \beta_{0,k} + 2\beta_{1,k} + \cdots + 2^{L-2}\beta_{L-2,k}. \tag{26}$$

The function $S(t)$ is given by

$$S(t) = \begin{cases} \dfrac{\sin\left(2\pi h q(t)\right)}{\sin \pi h}, & 0 \le t < LT, \\ \dfrac{\sin\left(\pi h - 2\pi h q(t - LT)\right)}{\sin \pi h}, & LT \le t < 2LT, \\ 0, & \text{otherwise.} \end{cases} \tag{27}$$

5.4. Receiver design

In [27], it is shown that an optimal CPM receiver can be built based on the Laurent linear representation and a Viterbi detector. Without going into details, we mention that sufficient statistics for the decision can be obtained by sampling at times nT the outputs of 2^{L-1} matched filters $C_k(-t)$; $k = 0, 1, \ldots, 2^{L-1} - 1$ simultaneously fed by the complex input $r(t)$.

As we aim at bit rates higher than 1 Gbps using low-power receivers, the complexity of this type of receivers is not acceptable. Fortunately, the Laurent approximation allows us to construct linear near-optimum MSK-type receivers. In (24), the pulse described by the component function $C_0(t)$ is the most important among all other components $C_k(t)$. Its duration is the longest ($2T$ more than any other component), and it conveys the most significant part of the energy of the signal. Kaleh [27] mentions the case of GMSK with $L = 4$, where more than 99% of the energy is contained in the main pulse $C_0(t)$. It is therefore a reasonable attempt to represent CPM using not all components, or even only one component. We study a linear receiver taking into account only the first Laurent pulse $C_0(t)$. According to (24), the sent signal $s(t)$ can thus be written as

$$s(t) = \sum_{n=0}^{N-1} e^{j\pi h\alpha_0[n]} C_0(t - nT) + \epsilon(t), \tag{28}$$

where $\epsilon(t)$ is a negligible term generated by the pulses $C_k(t)$; $k = 1, \ldots, 2^{L-1} - 1$. The received signal $r(t)$ can be written as

$$r(t) = s(t) \star h(t) + n(t), \tag{29}$$

where $h(t)$ is the linear multipath channel and $n(t)$ is the complex-valued AWGN. The equalization of the multipath channel is done with a simple zero-forcing filter $f_{\mathrm{ZF}}(t)$ assuming perfect channel knowledge. The output of the ZF filter can thus be written as

$$\hat{s}(t) = s(t) + n(t) \star f_{\mathrm{ZF}}(t). \tag{30}$$

Substituting (28) in (30), we get

$$\hat{s}(t) = \sum_{n=0}^{N-1} e^{j\pi h\alpha_0[n]} C_0(t - nT) + \epsilon(t) + n(t) \star f_{\mathrm{ZF}}(t). \tag{31}$$

The output $y(t)$ of the filter matched to $C_0(t)$ can now be written as

$$y(t) = \int_{-\infty}^{\infty} \hat{s}(s) \cdot C_0(s - t)ds, \tag{32}$$

and this signal sampled at $t = nT$ becomes

$$y[n] \stackrel{\mathrm{def}}{=} y(t = nT) = \int_{-\infty}^{\infty} \hat{s}(s) \cdot C_0(s - nT)ds. \tag{33}$$

Substituting (31) in (33), we get

$$y[n] = \sum_{m=0}^{N-1} e^{j\pi h\alpha_0[m]} \int_{-\infty}^{\infty} C_0(s - mT) \cdot C_0(s - nT)ds + \xi[n], \tag{34}$$

Table 5: System parameters OQPSK.

Filter bandwidth	BW = 1 GHz
Sample period	T = 1 ns
Number of bits per symbol	2
Number of symbols per block	256
Cyclic prefix length	64
Roll-off transmit filter	0.2

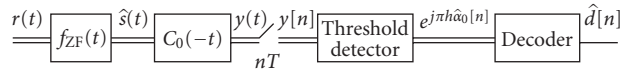

Figure 9: Linear GMSK receiver using the Laurent approximation.

where

$$\xi[n] = \int_{-\infty}^{\infty} \left[\epsilon(s) + n(s) \star f_{\mathrm{ZF}}(s)\right] \cdot C_0(s - nT)ds. \tag{35}$$

The linear receiver presented in [27] includes a Wiener estimator, as $C_0(t)$ extends beyond $t = T$ and thus causes intersymbol interference (ISI). When $h = 0.5$ though, $e^{j\pi h\alpha_0[m]} = j^{\alpha_0[m]}$ is alternatively purely real and purely imaginary, so the ISI in adjacent intervals is orthogonal to the signal in that interval. As the power in the autocorrelation of $C_0(t)$ at $t_1 - t_2 \geq 2T$ is very small, we can further simplify our receiver by neglecting the ISI. Equation (34) is indeed approximately:

$$y[n] \approx e^{j\pi h\alpha_0[n]} + \xi'[n]. \tag{36}$$

Thus we get an estimate of the complex coefficient $e^{j\pi h\hat{\alpha}_0[n]}$ of the first Laurent pulse $C_0(t)$ after the threshold detector. Taking into account the precoder (22), the Viterbi detection can now be replaced by a simple decoder [24]

$$\hat{d}[n] = j^{-n} \cdot e^{j\pi h\hat{\alpha}_0[n]}. \tag{37}$$

This linear receiver is shown in Figure 9.

6. NUMERICAL RESULTS

6.1. Simulation setup

6.1.1. Offset-QPSK with FDE

The system parameters of OQPSK are summarized in Table 5. The root-raised cosine transmit filter has a bandwidth of 1 GHz. The sample period after the insertion of the CP is 1 nanosecond. An OQPSK symbol carries the information of 2 bits. The CP length has been set to 64 samples, which is larger than the maximum channel time dispersion (around 40 nanoseconds). The transmitter filter has a roll-off factor of 0.2. This configuration enables a bit rate equal to 1.6 Gbps.

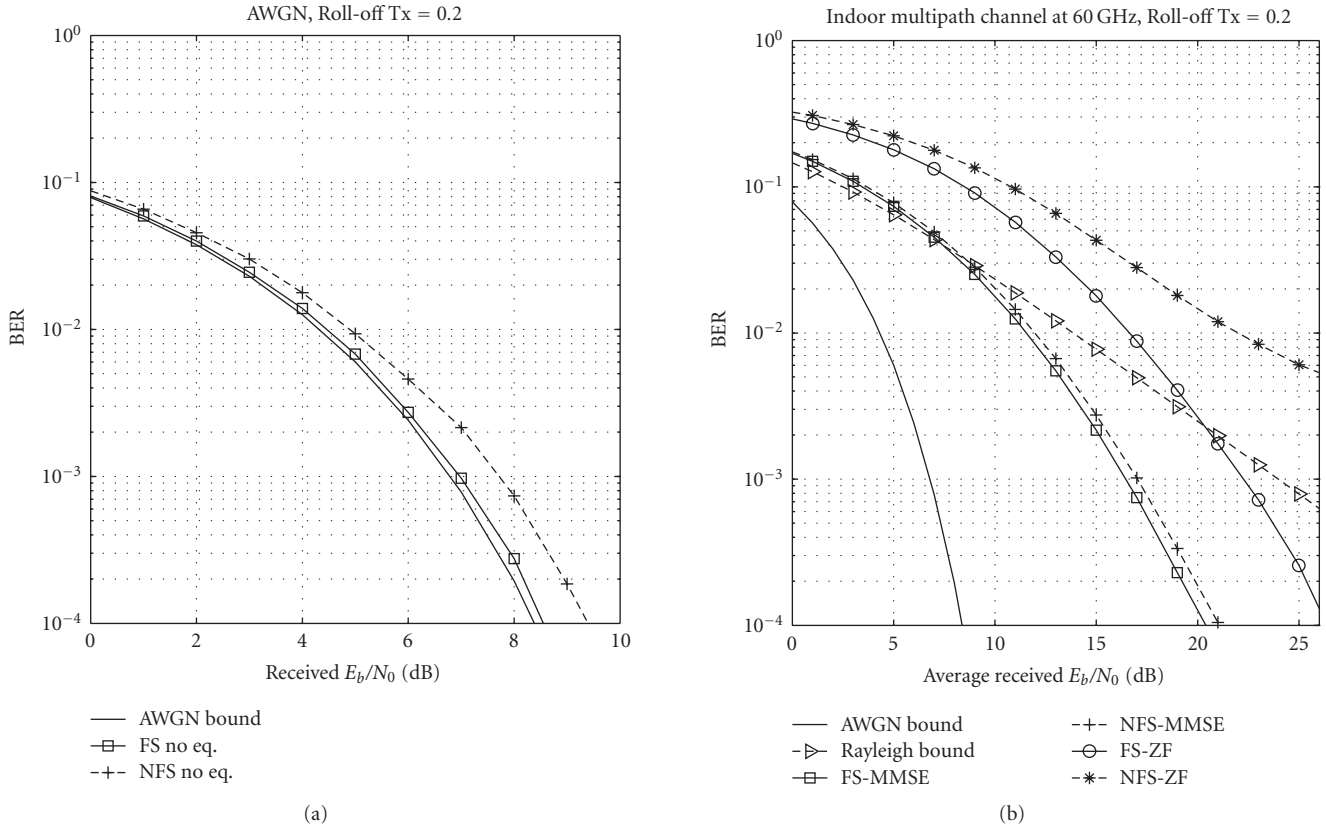

Figure 10: Uncoded BER performance of OQPSK with FDE for different receivers.

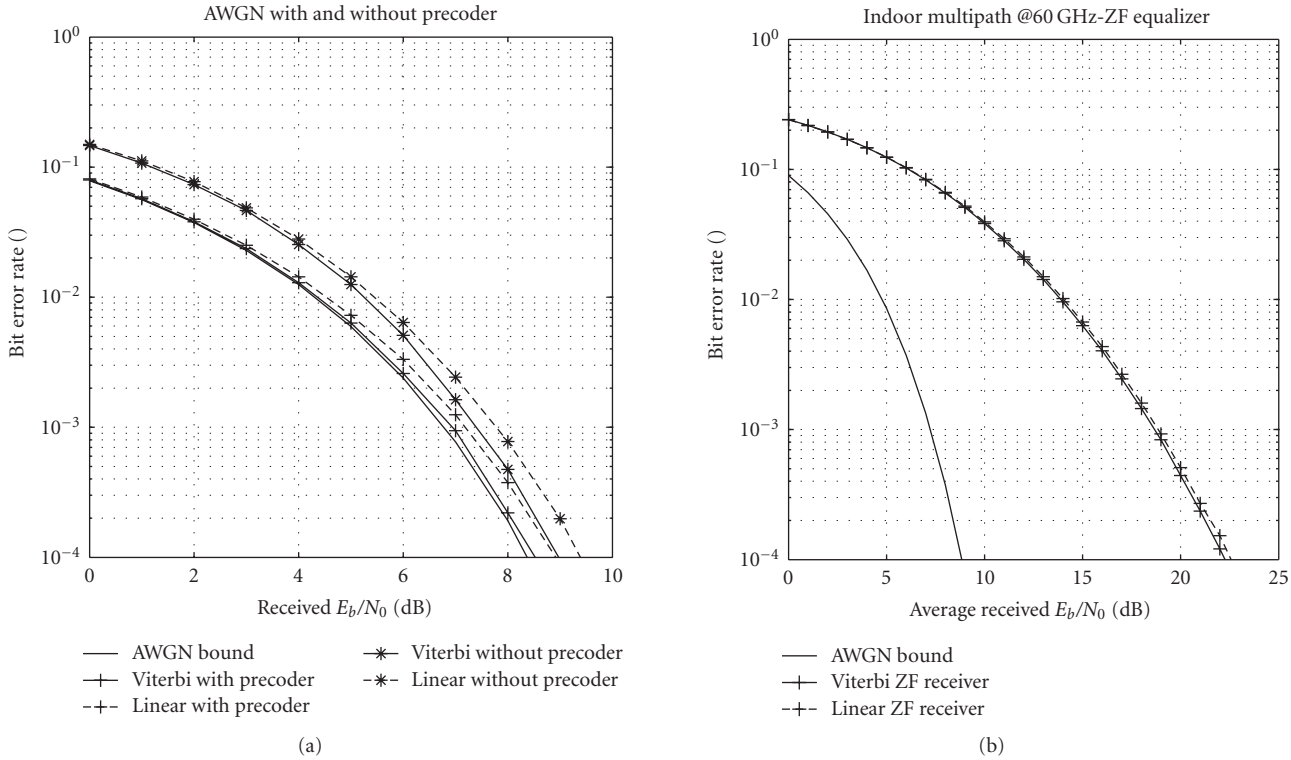

Figure 11: BER performance of CPM with ZF equalizer for different receivers.

Table 6: System parameters CPM.

Symbol duration	$T = 1$ ns
Pulse shape	Gaussian
Pulse duration	$3.T$
Modulation index	$h = 1/2$
Number of symbol levels	$M = 2$
Channel coding	Uncoded

6.1.2. CPM

The system parameters for CPM are summarized in Table 6. With these parameters, a bit rate of 1 Gbps is reached.

6.2. BER performance with ideal FE

6.2.1. OQPSK with FDE

We have compared the uncoded BER performance of the ZF and MMSE equalizers for both FS and NFS receivers. Simulation results are represented in Figure 10. In Figure 10(a), we show the BER performance in an AWGN channel. The simulation in an indoor frequency fading channel at 60 GHz is shown in Figure 10(b). One notices that the performance of FS receiver (solid line) is always better than that of NFS receivers (dashed line). In fact, in the NFS case, the frequency components of the transmitted signal above $0.5/T$ are filtered out by the anti-aliasing receiver filter, thus the received signal does not contain all the information from the transmitted signal. On the contrary, in the FS case, the anti-aliasing filter has a larger bandwidth than the transmitted signal, thus all the information from the transmitted signal is available in the received sampled signal.

Simulations show that the performance gain of FS over NFS receiver at a BER of 10^{-3} is about 0.5 dB with an MMSE equalizer. This gain is much higher with a ZF equalizer. In fact, the ZF equalizer is known to be very sensitive to nulls in the frequency domain. However, in the FS case, the performance is improved thanks to the diversity provided by the polyphase components. Thus, the probability that both the polyphase channels fall in a deep fade at the same time is reduced compared to the probability that only one of the channels fades.

ZF equalizers perform at least 5 dB worse at a BER of 10^{-3} relative to MMSE equalizers. However, even though the FS receivers yield better performance, they require an ADC with a sampling clock twice as fast as that needed by the NFS receivers. Moreover, the digital receiver is twice as complex as that of NFS receivers. Therefore, by trading-off complexity, cost and BER performance, the combination of NFS with MMSE is the most appropriate for low-cost low-consumption devices. We will thus use the NFS-MMSE receiver to assess the impact of FE nonidealities on the BER performance of OQPSK with FDE transceiver.

Notice that by comparing with the Rayleigh bound (solid triangle Figure 10(b)), it can also be verified that the SC modulation scheme with FDE inherently provides frequency diversity [5].

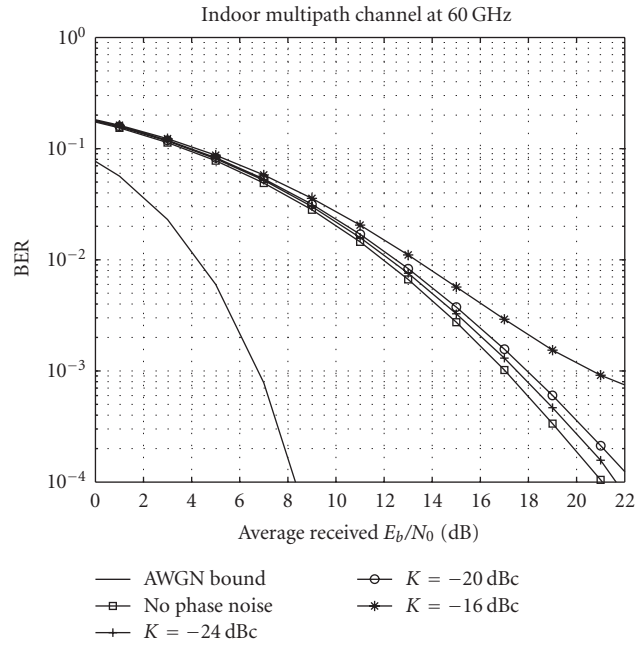

Figure 12: Impact of phase noise on BER performance of OQPSK.

6.2.2. CPM

Figure 11 shows the comparison of different GMSK receivers in AWGN and in a multipath 60 GHz scenario. In Figure 11(a), we compare the Viterbi and the linear receivers in AWGN, and show the theoretical BER bound as a reference. An obvious conclusion is that using a precoder delivers a gain of 0.5–1 dB with only a minor complexity increase. Next, we observe that using the linear receiver results in a loss of at most 0.5 dB compared to the Viterbi receiver. The complexity savings are huge though, so a linear receiver seems to be the right choice for 60 GHz applications.

In Figure 11(b), the BER performance in a 60 GHz indoor multipath environment is shown. The Viterbi and linear receiver, both with precoder and ZF equalizers, are compared. Here, the difference between both receivers almost completely vanishes. The linear receiver with ZF equalizer will be used to assess the impact of FE nonidealities on CPM.

6.3. Impact of phase noise on BER performance

6.3.1. OQPSK with FDE

We have simulated the BER performance of the NFS-MMSE receiver taking into account the phase noise. The simulations have been carried out in an indoor multipath environment at 60 GHz. Simulation results are represented in Figure 12. For a BER of 10^{-3}, the performance degradation is about 4 dB for an integrated PSD of -16 dBc. However, the performance can be improved by 3 dB when the integrated PSD is -20 dBc. That is at the price of more stringent requirements on VCO and synthesizer design.

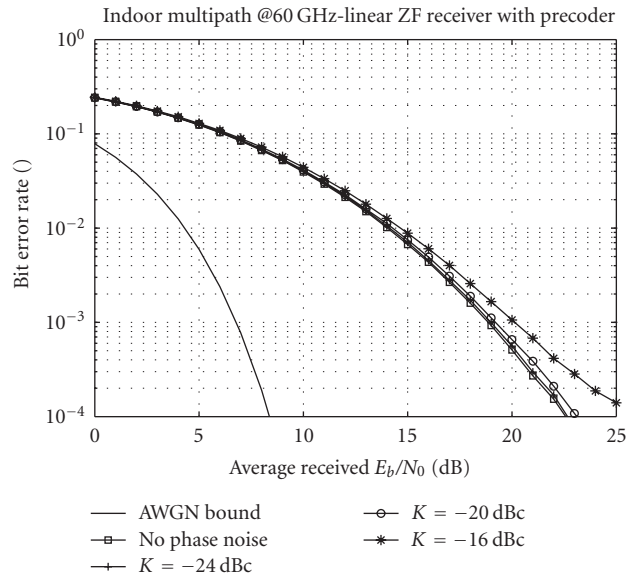

Figure 13: Impact of phase noise on the BER performance of CPM.

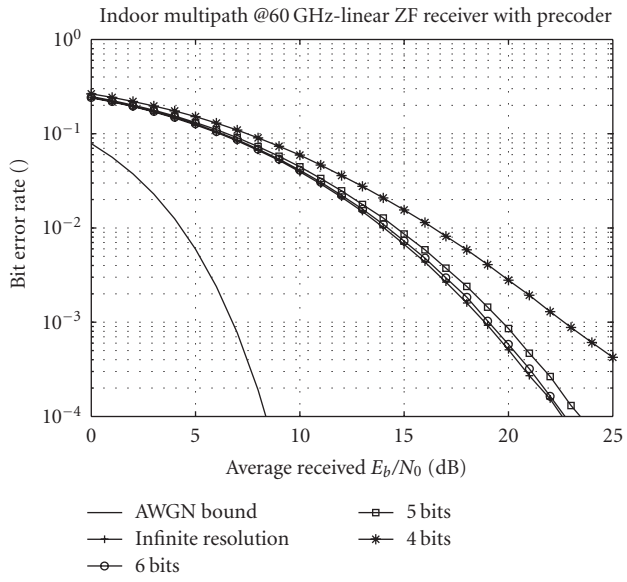

Figure 15: Impact of quantization on the BER performance of CPM.

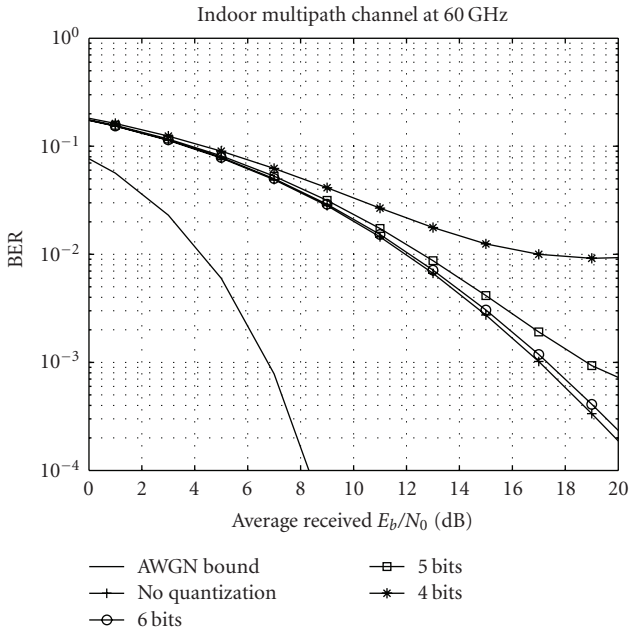

Figure 14: Impact of quantization on the BER performance of OQPSK.

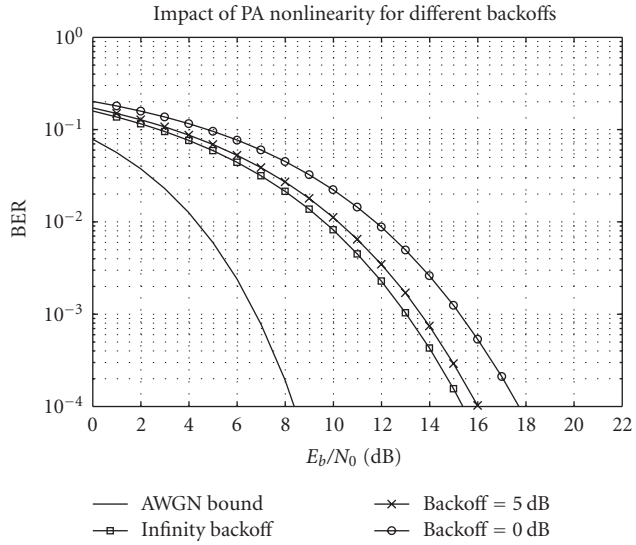

Figure 16: Impact of PA nonlinearity on BER performance of OQPSK.

6.3.2. CPM

Simulation results with PN in an indoor multipath environment at 60 GHz are presented in Figure 13. The performance degradation is negligible for an integrated PN power of -24 dBc. For a BER of 10^{-3}, we lose only slightly more than 1 dB with an integrated PN power of -16 dBc. CPM seems to be less sensitive to phase noise, or at least the effect of the multipath propagation, equalized with a ZF filter, drowns it out.

6.4. Impact of ADC nonidealities on BER performance

6.4.1. OQPSK with FDE

The impact of the resolution of the ADC in terms of bits is analyzed. Simulation results are represented in Figure 14. For a BER of 10^{-3}, the performance degradations are about 2 dB with an ADC of 5 bits. With one additional bit, the performance degradation becomes negligible. However, by increasing the number of resolution bits, the power consumption of the ADC will grow up.

6.4.2. CPM

Figure 15 shows the effect of quantization due to the ADC for CPM modulation. For a BER of 10^{-3}, the performance degradation is about 1 dB for an ADC with 5 bits. With an additional bit, performance degradation becomes negligible. CPM is less affected by a low resolution ADC than OQPSK.

6.5. Impact of PA nonlinearity on BER performance

Figure 16 shows the impact of inband distortion due to PA nonlinearity on the performance of OQPSK for different values of backoff. With a backoff of 5 dB, the performance degradation is only 0.5 dB for a BER of 10^{-3}. However, the power efficiency of the system is reduced. If the PA operates in the saturated region (0.5 dB backoff) to improve the power efficiency, then the performance degradation becomes 2 dB. Note that CPM is not affected by the nonlinearity in the PA thanks to its completely constant envelope.

7. CONCLUSION

In this paper, we compared the OQPSK and CPM modulators for communications at 60 GHz with a nonideal FE. For the OQPSK modulator, the NFS-MMSE receiver offers the best trade off between BER performance and complexity. Concerning the CPM modulator, the linear receiver offers a huge complexity reduction with only a minor performance degradation. The spectral efficiency of the OQPSK is higher than that of CPM. However, CPM is slightly less sensible to phase noise than OQPSK. The same conclusion applies to ADC resolution when the number of bits is less than 6. This is because the CPM signal after the multipath channel has a smaller envelope fluctuation than the OQPSK signal. For the same reason, CPM allows more power efficient operation of the PA while OQPSK needs a few dBs of backoff to avoid distortion.

REFERENCES

[1] http://www.ieee802.org/15/pub/TG3c.html.

[2] B. M. Motlagh, S. E. Gunnarsson, M. Ferndahl, and H. Zirath, "Fully integrated 60-GHz single-ended resistive mixer in 90-nm CMOS technology," *IEEE Microwave and Wireless Components Letters*, vol. 16, no. 1, pp. 25–27, 2006.

[3] P. F. M. Smulders and A. G. Wagemans, "Wide-band measurements of MM-wave indoor radio channels," in *Proceedings of the 3rd IEEE International Symposium on Personal, Indoor and Mobile Radio Communications (PIMRC '92)*, pp. 329–333, Boston, Mass, USA, October 1992.

[4] H. Yang, P. F. M. Smulders, and M. H. A. J. Herben, "Frequency selectivity of 60-GHz LOS and NLOS indoor radio channels," in *Proceedings of the 63rd IEEE Vehicular Technology Conference (VTC '06)*, vol. 6, pp. 2727–2731, Melbourne, Australia, May 2006.

[5] D. Falconer, S. L. Ariyavisitakul, A. Benyamin-Seeyar, and B. Eidson, "Frequency domain equalization for single-carrier broadband wireless systems," *IEEE Communications Magazine*, vol. 40, no. 4, pp. 58–66, 2002.

[6] C.-E. Sundberg, "Continuous phase modulation," *IEEE Communications Magazine*, vol. 24, no. 4, pp. 25–38, 1986.

[7] P. A. Laurent, "Exact and approximate construction of digital phase modulations by superposition of amplitude modulated pulses (AMP)," *IEEE Transactions on Communications*, vol. 34, no. 2, pp. 150–160, 1986.

[8] B. E. Rimoldi, "Decomposition approach to CPM," *IEEE Transactions on Information Theory*, vol. 34, no. 2, pp. 260–270, 1988.

[9] P. Smulders, "Exploiting the 60 GHz band for local wireless multimedia access: prospects and future directions," *IEEE Communications Magazine*, vol. 40, no. 1, pp. 140–147, 2002.

[10] C. R. Anderson and T. S. Rappaport, "In-building wideband partition loss measurements at 2.5 and 60 GHz," *IEEE Transactions on Wireless Communications*, vol. 3, no. 3, pp. 922–928, 2004.

[11] P. F. M. Smulders and L. M. Correia, "Characterisation of propagation in 60 GHz radio channels," *Electronics and Communication Engineering Journal*, vol. 9, no. 2, pp. 73–80, 1997.

[12] R. Davies, M. Bensebti, M. A. Beach, and J. P. McGeehan, "Wireless propagation measurements in indoor multipath environments at 1.7 GHz and 60 GHz for small cell systems," in *Proceedings of the 41st IEEE Vehicular Technology Conference (VTC '91)*, pp. 589–593, St. Louis, Mo, USA, May 1991.

[13] P. F. M. Smulders and G. J. A. P. Vervuurt, "Influence of antenna radiation patterns on MM-wave indoor radio channels," in *Proceedings of the 2nd International Conference on Universal Personal Communications*, vol. 2, pp. 631–635, Ottawa, Ont, Canada, October 1993.

[14] A. A. M. Saleh and R. A. Valenzuela, "Statistical model for indoor multipath propagation," *IEEE Journal on Selected Areas in Communications*, vol. 5, no. 2, pp. 128–137, 1987.

[15] J.-H. Park, Y. Kim, Y.-S. Hur, K. Lim, and K.-H. Kim, "Analysis of 60 GHz band indoor wireless channels with channel configurations," in *Proceedings of the 9th IEEE International Symposium on Personal, Indoor and Mobile Radio Communications (PIMRC '98)*, vol. 2, pp. 617–620, Boston, Mass, USA, September 1998.

[16] A. Bourdoux and J. Liu, "Transceiver nonidealities in multi-antenna systems," in *Smart Antennas—State of the Art*, chapter 32, pp. 651–682, Hindawi, New York, NY, USA, 2005.

[17] D. Dardari, "Exact analysis of joint clipping and quantization effects in high speed WLAN receivers," in *IEEE International Conference on Communications (ICC '03)*, vol. 5, pp. 3487–3492, Anchorage, Alaska, USA, May 2003.

[18] M. Engels, *Wireless OFDM Systems: How to Make Them Work?*, Kluwer Academic, Norwell, Mass, USA, 2002.

[19] C. Cao and K. O. Kenneth, "Millimeter-wave voltage-controlled oscillators in 0.13-/spl μ/m CMOS technology," *IEEE Journal of Solid-State Circuits*, vol. 41, no. 6, pp. 1297–1304, 2006.

[20] L. W. Couch II, *Digital and Analog Communication Systems*, Prentice Hall PTR, Upper Saddle River, NJ, USA, 6th edition, 2001.

[21] Z. Wang and G. B. Giannakis, "Wireless multicarrier communications," *IEEE Signal Processing Magazine*, vol. 17, no. 3, pp. 29–48, 2000.

[22] F. Horlin and L. Vandendorpe, "A comparison between chip fractional and non-fractional sampling for a direct sequence CDMA receiver," *IEEE Transactions on Signal Processing*, vol. 50, no. 7, pp. 1713–1723, 2002.

[23] A. Klein, G. K. Kaleh, and P. W. Baier, "Zero forcing and minimum mean-square-error equalization for multiuser detection in code-division multiple-access channels," *IEEE Transactions on Vehicular Technology*, vol. 45, no. 2, pp. 276–287, 1996.

[24] N. Al-Dhahir and G. Saulnier, "A high-performance reduced-complexity GMSK demodulator," *IEEE Transactions on Communications*, vol. 46, no. 11, pp. 1409–1412, 1998.

[25] K. Murota and K. Hirade, "GMSK modulation for digital mobile radio telephony," *IEEE Transactions on Communications Systems*, vol. 29, no. 7, pp. 1044–1050, 1981.

[26] J. G. Proakis, *Digital Communications*, McGraw-Hill, Boston, Mass, USA, 4th edition, 2001.

[27] G. K. Kaleh, "Simple coherent receivers for partial response continuous phase modulation," *IEEE Journal on Selected Areas in Communications*, vol. 7, no. 9, pp. 1427–1436, 1989.